

Development of time-varying global gridded T_s - T_m model for precise GPS-PWV retrieval

Peng Jiang^{1, 2}, Shirong Ye², Yin hao Lu¹, Yanyan Liu^{3, 2}, Dezhong Chen², Yanlan Wu¹

¹School of Resources and Environmental Engineering, Anhui University, Hefei, Anhui, China,

5 ²GNSS Research Center, Wuhan University, Wuhan, Hubei, China,

³Shenzhen Key Laboratory of Spatial Smart Sensing and Services, College of Civil Engineering, Shenzhen University, Shenzhen, Guangdong, China

Correspondence to: Peng Jiang (jiangpeng@ahu.edu.cn)

Abstract: Water-vapor-weighted mean temperature, T_m , is the key variable for estimating the mapping factor between GPS
10 zenith wet delay (ZWD) and precipitable water vapor (PWV). For the near real-time GPS-PWV retrieving, estimating T_m from
surface air temperature T_s is a widely used method because of its high temporal resolution and a fair degree of accuracy. Based
on the estimations of T_m and T_s at each reanalysis grid node of the ERA-Interim data, we analyzed the relationship between T_m
and T_s without data smoothing. The analyses demonstrate that the T_s - T_m relationship has significant spatial and temporal
variations. Static and time-varying global gridded T_s - T_m models were established and evaluated by comparisons with the
15 radiosonde data at 723 radiosonde stations in the Integrated Global Radiosonde Archive (IGRA). Results show that our global
gridded T_s - T_m equations have prominent advantages over the other globally applied models. At over 17% of the stations, errors
larger than 5 K exist in the Bevis equation (Bevis et al., 1992) and in the latitude-related linear model (Yao et al., 2014b), while
these large errors are removed in our time-varying T_s - T_m models. Multiple statistical tests at the 5 % significance level show
that the time-varying global gridded model is superior to the other models at 60.03 % of the radiosonde sites. The second-best
20 model is the $1^\circ \times 1^\circ$ GPT2w model, which is superior at only 12.86 % of the sites. More accurate T_m can reduce the contribution
of the uncertainty associated with T_m to the total uncertainty of GPS-PWV, and the reduction augments with the growth of
GPS-PWV. Our theoretical analyses with high PWV and small uncertainty in surface pressure indicate that the uncertainty
associated with T_m can contribute more than 50 % of the total GPS-PWV uncertainty by using the Bevis equation, and it can
decline to less than 25 % by using our time-varying T_s - T_m model. However, the uncertainty associated with surface pressure
25 dominates the error budget of PWV (more than 75 %) when the surface pressure has error larger than 5 hPa. GPS-PWV
retrievals using different T_m estimates were compared at 74 International GNSS Service (IGS) stations. At 74.32% of the IGS
sites, the relative differences of GPS-PWV are within 1 % by applying the static or the time-varying global gridded T_s - T_m
equations, while the Bevis model, the latitude-related model and the GPT2w model perform the same at respectively 37.84 %,
41.89 % and 29.73 % of the sites. Compared with the radiosonde PWV, the error reduction in the GPS-PWV retrieval by using
30 a more accurate T_m parameterization can be around 1~2 mm, which accounts for around 30 % of the total GPS-PWV error.

1. Introduction

Water vapor is an important trace gas and one of the most variable components in the troposphere. The transport, concentration, and phase transition of water vapor are directly involved in the atmospheric radiation and hydrological cycle. It plays a key role in many climate changes and weather processes (Adler et al., 2016; Mahoney et al., 2016; Song et al., 2016).
 35 However, water vapor has high spatial-temporal variability, and its content is often small within the atmosphere. It is a challenge to measure water vapor content accurately and timely. For decades, several methods have been studied, such as radiosondes and water vapor radiometers, sun photometers, and GPS (Campmany et al., 2010; Ciesielski et al., 2010; Liu et al., 2013; Perez-Ramirez et al., 2014; Li et al., 2016). Compared with the traditional water vapor observations, ground-based
 40 GPS water vapor measurement has the advantages of high accuracy, high spatial-temporal resolution, all-weather availability, and low-cost (Haase et al., 2003; Pacione and Vespe, 2008; Lee et al., 2010; Means, 2013; Lu et al., 2015). Ground-based GPS water vapor products, mainly including precipitable water vapor (PWV), are widely used in many fields such as real-time vapor monitoring, weather and climate research, and numerical weather prediction (NWP) (Van Baelen and Penide, 2009; Karabatic et al., 2011; Rohm et al., 2014; Adams et al., 2017).

GPS observations require some kinds of meteorological elements to estimate PWV. Zenith hydrostatic delay (ZHD) can
 45 be calculated using surface pressure P_s by equation (Ning et al., 2013) :

$$ZHD = (2.2767 \pm 0.0015) \frac{P_s}{f(\varphi, H)} \quad (1)$$

where φ is the latitude, H is the geoid height in meters, and

$$f(\lambda, H) = (1 - 2.66 \times 10^{-3} \cos \varphi - 2.8 \times 10^{-7} H) \quad (2)$$

Then, zenith wet delay (ZWD) is generated by subtracting ZHD from zenith total delay (ZTD). ZTD can be directly
 50 estimated from precise GPS data processing. Finally, a conversion factor Q , which is used to map ZWD onto PWV, is determined by the water-vapor-weighted mean temperature T_m over a GPS station. The mapping function from ZWD to PWV is expressed as (Bevis et al., 1992):

$$PWV = \frac{ZWD}{Q} = \frac{ZTD - ZHD}{Q} \quad (3)$$

and Q is computed using following formula:

$$Q = 10^{-6} \rho_w R_v \left[(k_3 / T_m) + k_2' \right] \quad (4)$$

where ρ_w is the density of liquid water, R_v is the specific gas constant for water vapor, $k_2' = (22.1 \pm 2.2) \text{K} \cdot \text{mbar}^{-1}$ and $k_3 = (3.739 \pm 0.012) \times 10^5 \text{K}^2 \cdot \text{mbar}^{-1}$ are physical constants (Ning et al., 2016). T_m is the weighted mean temperature which

is defined as a function related to the temperature and water vapor pressure. It can be approximated as the following formula (Bevis et al., 1992):

60

$$T_m = \frac{\int \frac{e}{T} dz}{\int \frac{e}{T^2} dz} \approx \frac{\sum_{i=1}^n \frac{e_i}{T_i} \Delta z_i}{\sum_{i=1}^n \frac{e_i}{T_i^2} \Delta z_i} \quad (5)$$

where e and T respectively represent vapor pressure in hPa and temperature in Kelvin, i denotes the i th level and Δz_i is the height difference of i th level. Vapor pressure e is calculated using equation $e=e_s \times RH$; RH is the relative humidity, and the saturation vapor pressure e_s can be estimated from the temperature observations using Goff-Gratch formula (Sheng et al., 2013).

65

There are three main approaches to estimate T_m . They have respective advantages and disadvantages when they are applied for different purposes:

70

(1) The integration of vertical temperature and humidity profiles are believed to be the most accurate method. The profile data can be extracted from radio soundings or NWP datasets (Wang et al., 2016). However, some inconveniences have to be endured. It usually takes considerable amounts of time to acquire the NWP data, which is normally released with large volumes every 6 hours. This limits the use of NWP data in the near real-time GPS-PWV retrieving. Radiosonde data is another profile data source, but it has low spatial and temporal resolution. At most of the radiosonde sites, sounding balloons are daily cast at 00:00 UTC and 12:00 UTC. Furthermore, a large amount of GPS stations are not located close enough to the radio sounding sites. Therefore, such methods are appropriate for climate research or the study of long-term PWV trends, but do not meet the real-time requirements.

75

(2) Several global empirical models of T_m are established based on the analyses of T_m time series from NWP datasets or other sources (Yao et al., 2012; Chen et al., 2014; Bohm et al., 2015). T_m at any time and any location can be estimated from these models. They are often independent of the current meteorological observations which are required to be observed together with the GPS data. However, some important real variations, which may be dramatic during some extreme weather events, can be lost without the constraints of current real data (Jiang et al., 2016). Therefore, these modeled estimates are not accurate enough for high-precision meteorological applications, such as providing GPS-PWV estimates for weather prediction.

80

(3) Many studies indicated that the T_m parameter has a relationship with some surface meteorological elements, such as surface air temperature or surface air humidity (Bevis et al., 1992; Yao et al., 2014a). These surface meteorological parameters can be measured accurately and rapidly. T_m is then estimated using these surface measurements. However, these studies also revealed that the relationships are often weak, except the T_s - T_m relationship. For example, Bevis et al. (1992) introduced the equation $T_m=0.72 T_s+70.2$ [K] after analyzing 8712 radiosonde profiles collected at 13 sites in the U.S. over two years. This equation has been widely used in many other studies.

85

According to Rohm et al. (2014), GPS-ZTD can be estimated very precisely by real-time GPS data processing. This means that T_m is one of the key parameters in the near real-time GPS-PWV estimation. On the other hand, method (3) is the most suitable method for estimating T_m in near real-time because of its balance between timeliness and accuracy. The T_s - T_m relationship has spatial-temporal variations. Several regional T_s - T_m equations were established using the profile data over corresponding fields (Wang et al., 2012). However, a T_s - T_m model without spatial variation is not good enough for a vast field, e.g. the Indian region (Singh et al., 2014). Aside from this, some vast areas have no specific high-precision T_s - T_m model, for example over the oceans. In general, significant differences exist between oceanic and terrestrial atmospheric properties, especially near the surface layer and within the boundary layer. The change of T_s from land to ocean may be very different from that of T_m . Therefore it is necessary to model the T_s - T_m relationship over oceanic regions, since several ocean-based GPS meteorology experiments demonstrated the potential of such technique to retrieve PWV over the broad ocean (Rocken et al., 2005; Kealy et al., 2012). A global gridded T_s - T_m model has been established by Lan et al. (2016). In this model, the $2.0^\circ \times 2.5^\circ$ T_m data from “GGOS Atmosphere” and the $0.75^\circ \times 0.75^\circ$ T_s data from the European Centre for Medium-Range Weather Forecasts (ECMWF) reanalysis data are both smoothed to the resolution of $4^\circ \times 5^\circ$. However, the T_s - T_m relationship is varying in time (Yao et al., 2014a), while the Lan et al. (2016) model is static.

The objective of this study is mainly to (1) develop global gridded T_s - T_m models without any smoothing of the data, then assess their precision, and (2) study the performances of GPS-PWV retrievals using our T_s - T_m models. Table 1 lists the main differences between the T_s - T_m model developed in this study and the other global used T_m models. In section 2, the data sources and determining methods of T_m are introduced in detail. Then, in section 3 we analyze the T_s - T_m relationships and their variations on a global scale. Global-gridded T_s - T_m estimating models in different forms are established and evaluated in section 4. Section 5 assesses the accuracies of different PWV retrievals and section 6 presents conclusions based on our experiments.

Table 1. Main differences between T_s - T_m models developed in this study and other global used T_m estimation models

Strategies T_s - T_m Models	Bevis model (Bevis et al., 1992)	Latitude-related linear model (Yao et al., 2014b)	Global-gridded model (Lan et al., 2016)	Time-varying global gridded model (our study)	GPT2w model (Bohm et al., 2015)
Applicable Regions	Regional/Global	Global	Global	Global	Global
Data Sources	Radiosonde	T_s from the $0.75^\circ \times 0.75^\circ$ ERA-Interim, and T_m from the $2^\circ \times 2.5^\circ$ “GGOS Atmosphere”	T_s from the $0.75^\circ \times 0.75^\circ$ ERA-Interim, and T_m from the $2^\circ \times 2.5^\circ$ “GGOS Atmosphere”	T_s and T_m both from the $0.75^\circ \times 0.75^\circ$ ERA-Interim	T_m from the $1^\circ \times 1^\circ$ ERA-Interim monthly mean data
Data Processing	Integrate radiosonde profiles	$4^\circ \times 5^\circ$ Sliding window smooth	$4^\circ \times 5^\circ$ Sliding window smooth	Integrate ERA-Interim profiles	Integrate ERA-Interim profiles
Variations in model	Static without any variations	Spatial variations depend on only latitude (15° latitude interval), but no temporal variations	$4^\circ \times 5^\circ$ global gridded, but no temporal variations	$0.75^\circ \times 0.75^\circ$ global gridded and considering time variations	$1^\circ \times 1^\circ$ global gridded, considering time variations, but independent of

					current surface observations
--	--	--	--	--	------------------------------

2. Data Sources and Methodology

As the definition of T_m in equation (5), e_i parameter at the middle height of i th level is calculated by vertically exponential interpolation of the water vapor pressure of its two neighbor measurement points. The temperature is estimated by linear interpolation of the two neighbor temperatures. The integral intervals are from the earth surface to the top level of profile data. The height of top level depends on the data sources we employed. The essential profile data, including the temperature, height and relative humidity values through the entire atmospheric column, can be obtained from the radiosondes or NWP datasets.

We employed radiosonde data from the Integrated Global Radiosonde Archive (IGRA, <ftp://ftp.ncdc.noaa.gov/pub/data/igra>) to calculate T_m . Version 2.0 of the IGRA-derived sounding parameters provides pressure, geopotential height, temperature, saturation vapor pressure, and relative humidity observations at the observed levels. Bias may be introduced if the integrals were terminated at lower levels (Wang et al., 2005), thus the integrations were performed up to the topmost valid radiosonde data. According to our quality control processes, some radiosonde profile data were rejected. In each profile, the surface observations must be available and the top profile level should not be lower than 300 hPa standard level. Furthermore, the level number between the surface and the top level should be greater than 10 to avoid too sparse vertical profiles. At most of the radio sounding stations, sounding balloons are launched every 12 hours, and their ascending paths are assumed to be vertical.

Profile data are usually provided by NWP products at certain vertical levels. The ERA-Interim product from ECMWF provides data on a regular 512 longitude by 256 latitude N128 Gaussian grid after the grid transforming performed by the NCAR Data Support Section (DSS). On each grid node of ERA-Interim, temperature, relative humidity and geopotential at 37 isobaric levels from 1000 hPa to 1 hPa can be obtained. Dividing the geopotential by constant gravitational acceleration value ($g \approx 9.80665 \text{ m/s}^2$), we can determine the geopotential heights of the surface and levels. Datasets are available at 00:00, 06:00, 12:00 and 18:00 UTC every day and have been covering a period from 1979.01 to present.

In theory, the computation of equation (5) should be integrated through the entire atmospheric column, and the geopotential height should be converted to the geometric height. However, water vapor is solely concentrated in the troposphere, and most of it is specifically located within the first 3 kilometers above sea-level. Moreover, in the two selected datasets, the geopotential heights of top pressure levels are approximately 30~40 km. Geopotential height is very close to geometric height in such height ranges. According to our computation, the relative difference between them is only between 0.1 %~0.9 %. In fact, the height difference Δz can be replaced by the geopotential height difference Δh in equation (5), since the division can almost eliminate the difference between the two different height types. The T_m value nearly has no change after such height replacement. For the convenience of calculation, we directly employed the geopotential height

variable. In this paper, we denoted the T_m derived from ERA-Interim as T_{m_ERA} .

At each reanalysis grid node, the computation of equation (5) always starts from the surface height to the top pressure level. The pressure levels below surface height were rejected. T_s is defined as the variable of “temperature at 2 meters above ground”, and surface water vapor pressure can be derived from the “2 meter dewpoint temperature” variable in ERA-Interim.

140 These T_s were also used in the regression analyses between T_s and T_m .

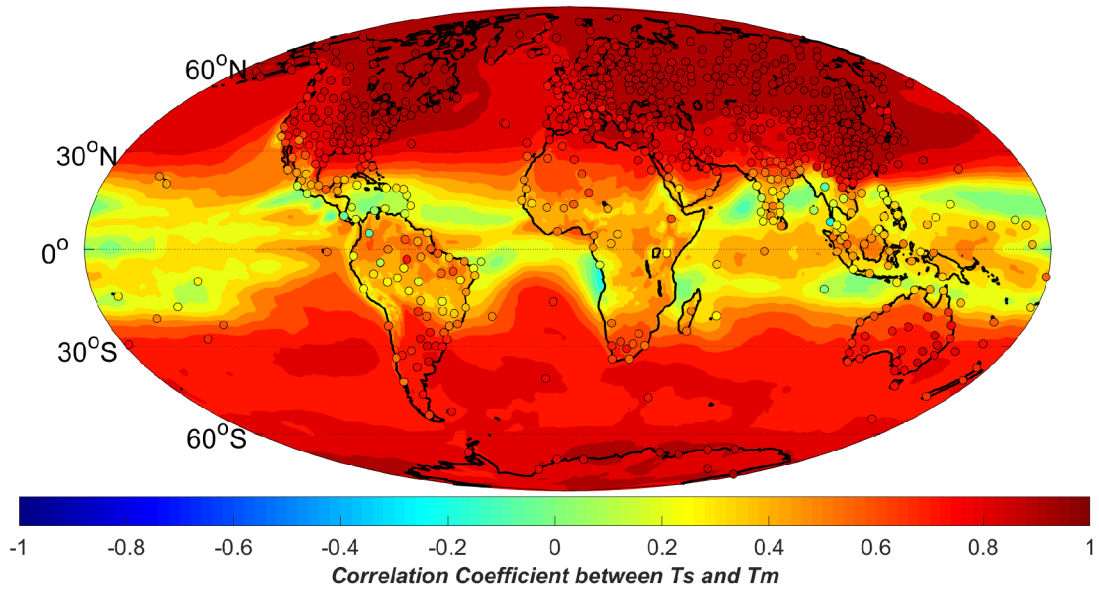
3. Correlation between T_s and T_m

Many studies have indicated the close relationship between T_s and T_m . However, T_m is also found not being closely related to T_s in some regions, e.g., in the Indian zone (Raju et al., 2007). Using the T_m and T_s generated from the global gridded reanalysis data, we are able to study the T_s - T_m relationship in detail.

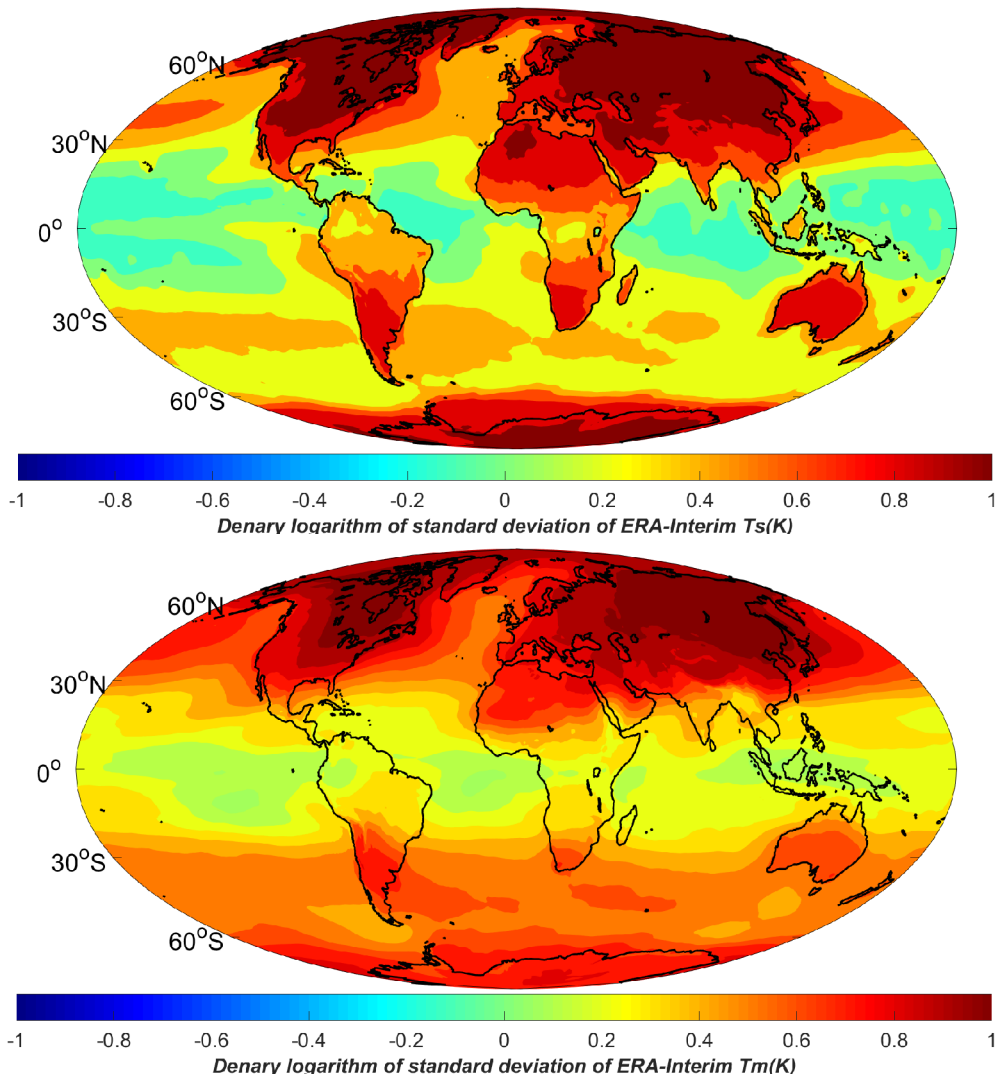
145 We first carried out a linear regression analysis on four years of T_s and T_m data generated from the radiosonde data and the global gridded ERA-Interim datasets, with data covering the period 2009\01 to 2012\12. The analysis results are shown in figure 1. Although the two datasets have different temporal resolutions (12 hours for the radiosonde data and 6 hours for the ERA-Interim data) and spatial resolutions, both analyses agree well with each other. This is expected because the radiosonde data have been assimilated into the ERA-Interim products. Our analyses also indicate that the T_s - T_m correlation coefficient is generally related to the latitude. The same conclusion has been drawn in other studies (Yao et al., 2014b). Significant positive correlation coefficients can be found at mid- and high- latitudes and reach a maximum in the polar regions. The correlation coefficients drop dramatically at low latitudes. This is because T_m is stable there, showing independency of the other parameters. To study the variations of T_s and T_m , we illustrated the denary logarithm values of their standard deviations in figure 2. It is evident that T_m varies to a lesser degree than T_s at low latitudes. Aside from the latitude-related features, there are obvious differences of the T_s - T_m correlation coefficients between land and ocean. We even found that negative correlation coefficients over certain oceans, e.g., low-latitude Western Pacific, Bay of Bengal or Arabian Sea (see figure 1). Unreliable regression analysis results may be derived when the T_s and T_m data both have small variations. In figure 3, scatter plots of T_s and T_m from ERA-Interim at two locations 0.35° N 180.00° E and 70.53° N 180.00° E are given. As the blue dots show, the T_s - T_m relationship is weak in the areas near the equator, because the entire variation ranges of T_s and T_m are both within 10 K. This results in a meaningless linear regression (see the magenta line). The T_s - T_m correlation coefficient is only -0.0893 there. Other than the large spatial variations, studies have revealed that the T_s - T_m relationship also has temporal variations (Wang et al., 2005). Therefore, a good T_s - T_m model should take both the spatial and temporal variations into consideration, and this is the main aim in the following sections.

150

160



165 **Figure 1: Correlation coefficients between T_s and T_m generated from radiosonde data (dots) and ERA-Interim reanalysis datasets (color-filled contours) over a period of 4 years from 2009 to 2012.**



170 **Figure 2: Denary logarithm of the standard deviation of (top) T_s and (bottom) T_m generated from the ERA-Interim data covering the year 2009 to 2012. Temperature unit is Kelvin.**

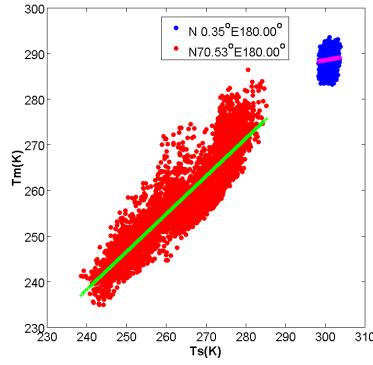


Figure 3: T_s - T_m scatter plots at two locations: (blue dots) 0.35° N 180.00° E and (red dots) 70.53° N 180.00° E, the magenta and green lines are their linear fitting curves. Temperature unit is Kelvin.

4. Development of global-gridded T_s - T_m models

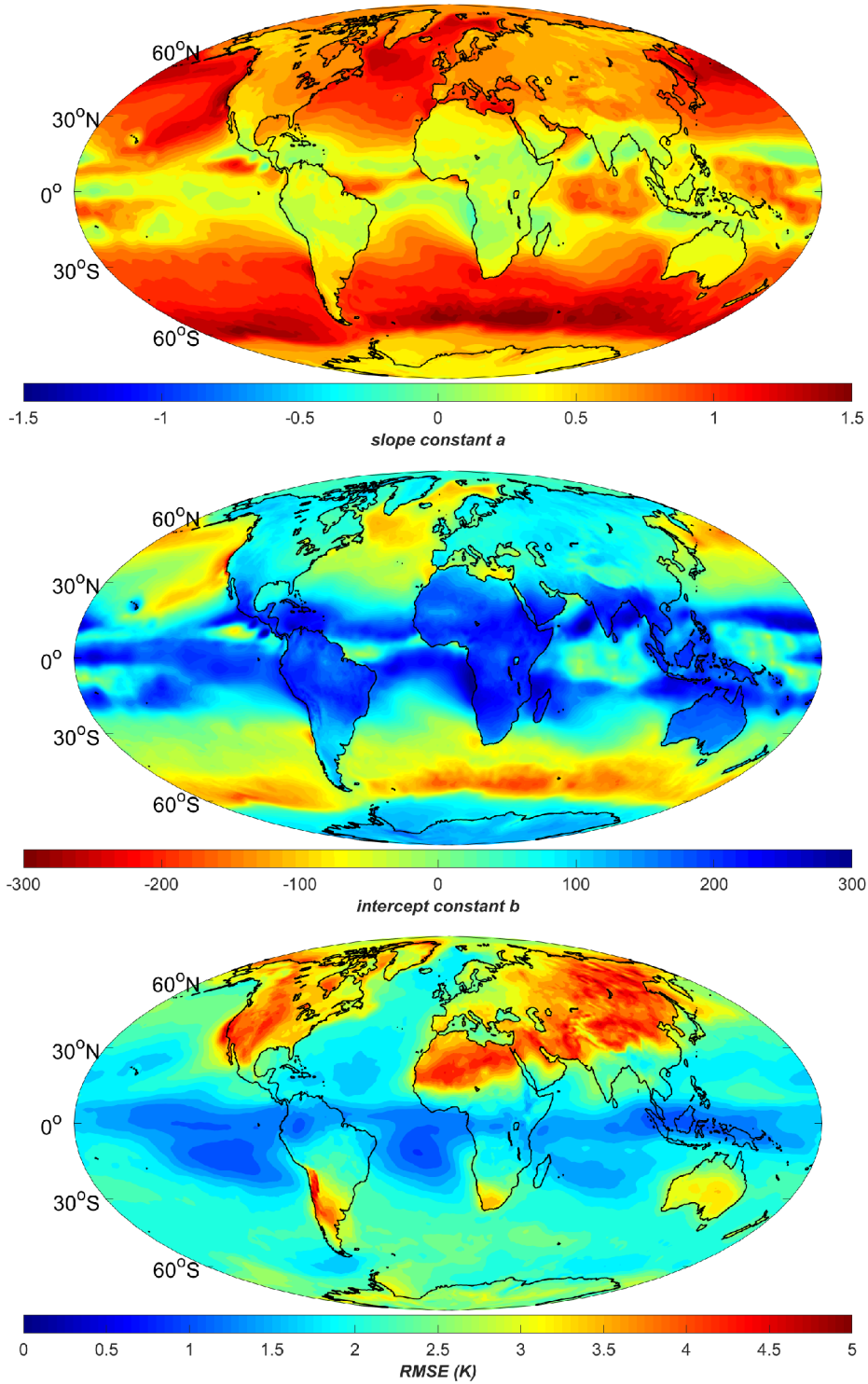
175 Since the T_s - T_m relationship has large spatial variations, a global gridded T_s - T_m model is preferred for precise GPS-PWV estimations. In this section, a static global gridded model and a time-varying global gridded model are established and assessed.

4.1 Static global-gridded T_s - T_m model

A linear formula $T_m = aT_s + b$ for the relation between T_m and T_s has been adopted in many studies. Based on the T_s and T_m products from the ERA-Interim data covering the year 2009 to 2012, we performed linear fittings of T_m versus T_s on each grid point. Then, the slope constant (a), the intercept constant (b) and the fitting root mean square error (RMSE) of each linear expression were calculated and contoured in figure 4. The a and b values are related to the latitude as well as the underlying surface (e.g. land, ocean). In the mid-high latitudes over the Northern Hemisphere, constant a value varies from 0.6 to 0.8, and constant b is approximately 100~50 over most of the continents. The constants in the Bevis equation are within these value ranges. Constant a is smaller (approximately 0.5~0.7) over land at the mid to high latitudes over the Southern Hemisphere.

185 Especially, there are abrupt changes in the values of constants a and b from land to ocean at the mid to high latitudes due to the different variation features of T_s and T_m (see figure 2). At the low latitudes, the a value is smaller than over the other regions, because of the low variations of T_s and T_m . The fitting RMSEs are within 2~4 K over the mid to high latitude lands, and lower values are obtained over the oceans or at the low latitudes. The reason for the low RMSE around the equator is the smaller fluctuation of T_m . Meanwhile, there is no RMSE larger than 4.5 K in the results of our model. As we did not perform any

190 spatial or temporal smoothing of the data during the data processing, both the precision and resolution of our static model is better than other models (e.g. Lan et al., 2016).



195 **Figure 4: Distributions of the (top) slope constant a , (middle) intercept constant b , and (bottom) RMSE of static linear T_s-T_m equations at ERA-Interim grid nodes. Temperature unit is Kelvin.**

4.2 Time-varying global-gridded T_s-T_m model

The time variation of T_s-T_m relationship should also be considered in a precise T_s-T_m model. Therefore, a time-varying equation is applied for T_s-T_m regression at each grid node:

200

$$T_m = aT_s + b + m_1 \cos\left(\frac{doy}{365.25}2\pi\right) + m_2 \sin\left(\frac{doy}{365.25}2\pi\right) + n_1 \cos\left(\frac{doy}{365.25}4\pi\right) + n_2 \sin\left(\frac{doy}{365.25}4\pi\right) + p_1 \cos\left(\frac{hr}{12}\pi\right) + p_2 \sin\left(\frac{hr}{12}\pi\right) \quad (6)$$

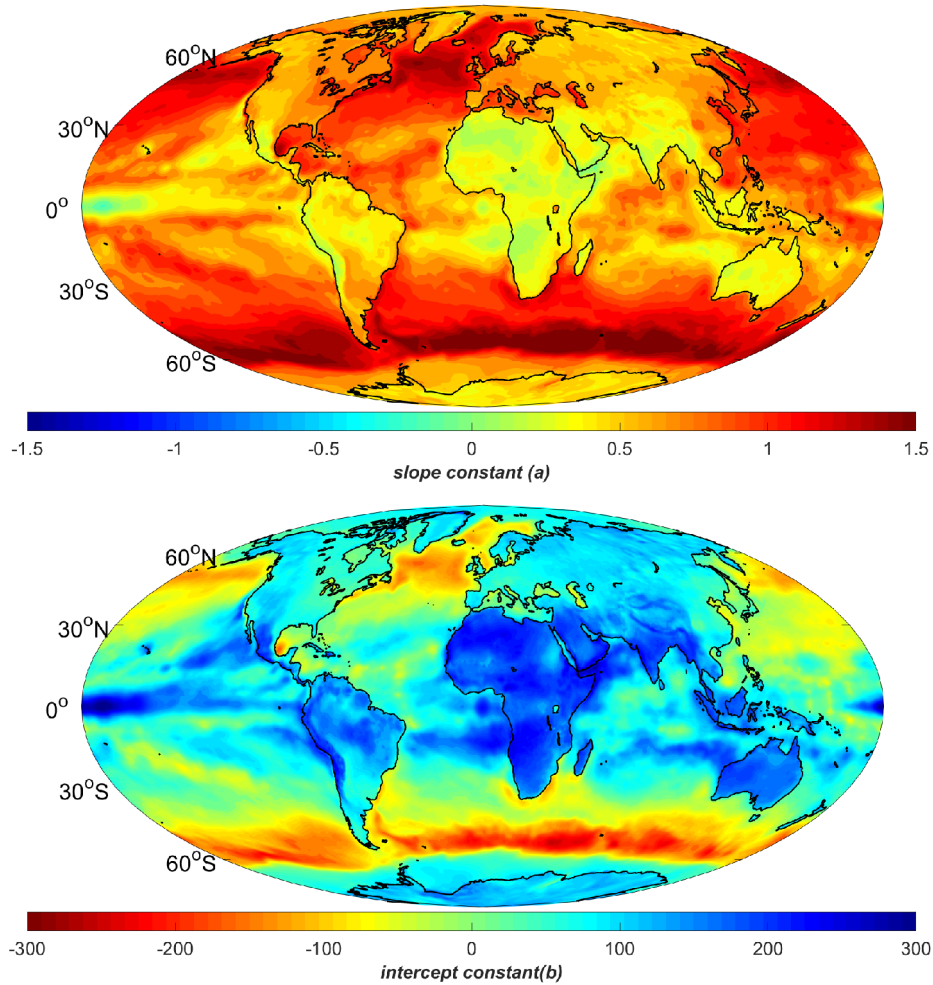
where *doy* represents the observed day of year and *hr* is the observed hour in UTC time; (m_1, m_2), (n_1, n_2) and (p_1, p_2) are fitting coefficients. These equations can reflect the amplitudes of annual, semiannual and diurnal variations in our T_s - T_m models.

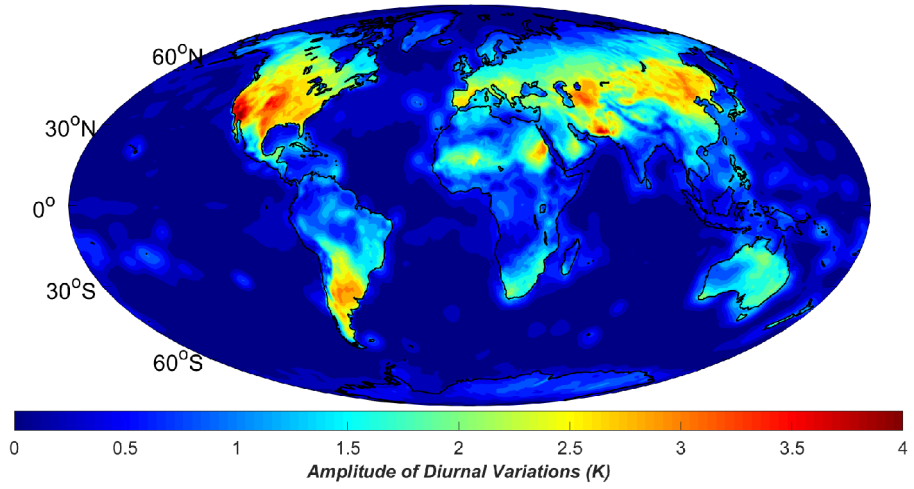
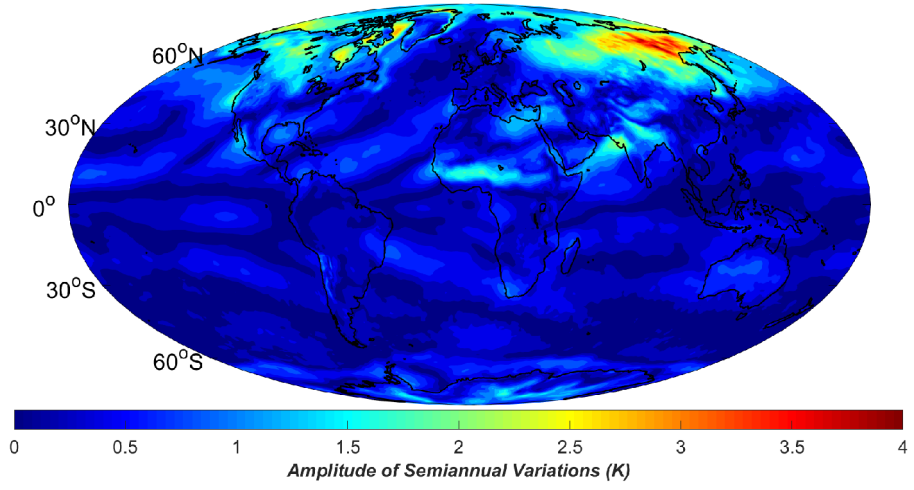
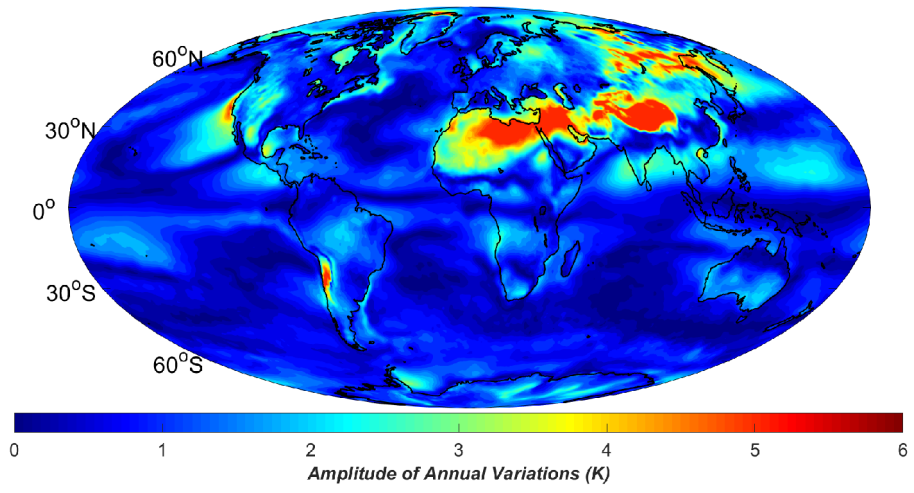
205

Our new regression model found similar values for the coefficients a and b (of its static term) as for the static model in section 4.1, except for some differences over the oceans. In figure 5, besides these constants a and b , we also illustrate the amplitudes of annual, semiannual, and diurnal terms. We can see that there are large annual variations (amplitude > 5 K) in the vast regions from Tibet to North Africa, and in some places of the Siberia and Chile. Large diurnal variations (amplitude > 3 K) mainly occur over the mid-latitude lands such as Northeast Asia or North America. Semiannual variations, however, are small in most of areas except some high-latitudes (amplitude > 3 K). All variations are smaller over the oceans due to the slower temperature changes over water than over land. The estimated T_m RMSE is also contoured in figure 5, and we can see

210

that the RMSE dropped significantly in the regions with large annual or diurnal variations.





215

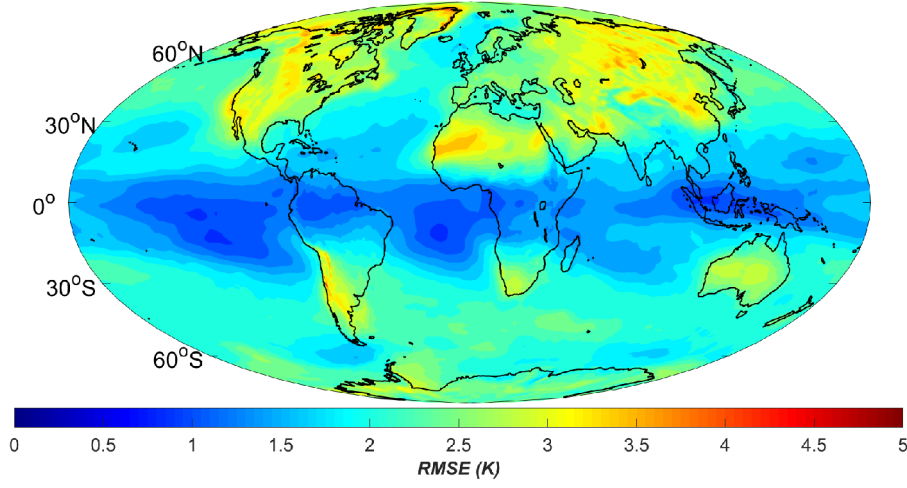


Figure 5: (top) The slope constant a , (second) intercept constant b , amplitudes of T_m (third) annual, (forth) semiannual and (fifth) diurnal terms in our time-varying global gridded $T_s - T_m$ model, and (bottom) the model estimated T_m RMSE distribution. Temperature unit is Kelvin.

4.3 Assessments of $T_s - T_m$ models

To further assess the precision of the $T_s - T_m$ models using other independent data sources, we generated T_m and T_s from the radiosonde data at 723 radiosonde stations in the year 2016. These data are not assimilated into the 2009~2012 ERA-Interim datasets. As a result, we can regard them as independent of our model. At each radiosonde site, different $T_s - T_m$ models were employed to calculate T_m . In addition, we also estimated T_m using the $1^\circ \times 1^\circ$ GPT2w model (Bohm et al., 2015), which is a global gridded T_m empirical model independent of the surface meteorological observation data. Then, these calculated T_m will be evaluated by comparing them with the integrated T_m of radiosondes (denoted as T_{m_RS}) twice a day.

The model estimations of T_m are denoted as T_{m_Bevis} , T_{m_LatR} , T_{m_static} , $T_{m_varying}$, and T_{m_GPT2w} from respectively the Bevis equation, the latitude-related model, our static global gridded model, time-varying global gridded model, and the GPT2w model. When the global gridded models are employed, the radiosonde station may not be located at a grid node. Therefore, we interpolated the coefficients in the $T_s - T_m$ equations from the neighboring grids to the radiosonde sites. The interpolation formula is expressed as (Jade and Vijayan, 2008) :

$$C_{site} = \sum_{i=1}^4 w^i C_{grid}^i \quad (7)$$

C_{site} and C_{grid}^i represent the coefficients in $T_s - T_m$ equations at the radiosonde site location and its neighboring grids, respectively.

w^i are the interpolation coefficients, which are determined using the equation:

$$w^i = \frac{(R\psi^i)^{-\lambda}}{\sum_{j=1}^4 (R\psi^j)^{-\lambda}} \quad (8)$$

where $R=6378.17$ km is the mean radius of the earth, λ is the scale factor which equals one in our study, and ψ^i is the

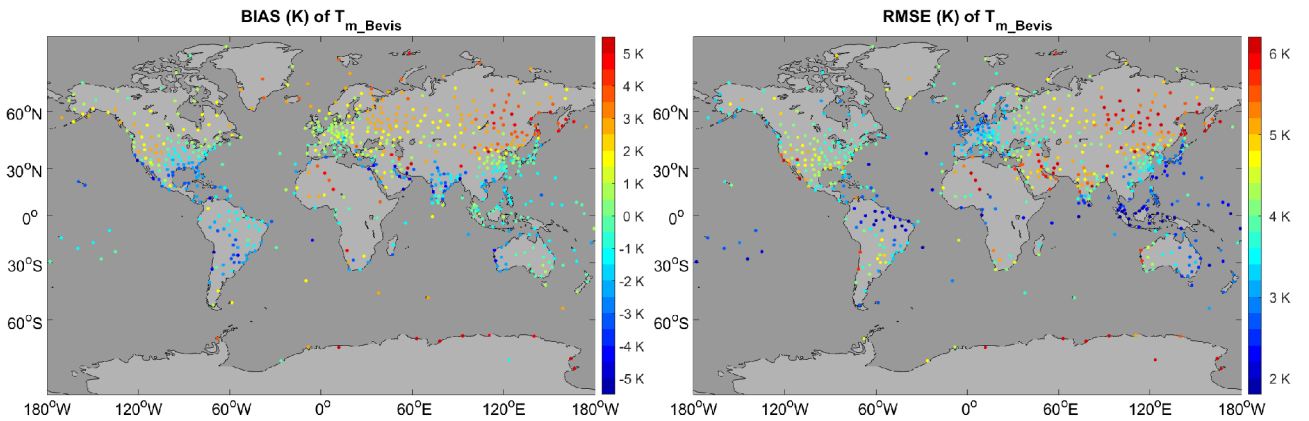
angular distance between the i th grid node and the station's position. ψ^i are computed using following formula (with latitude φ and longitude θ):

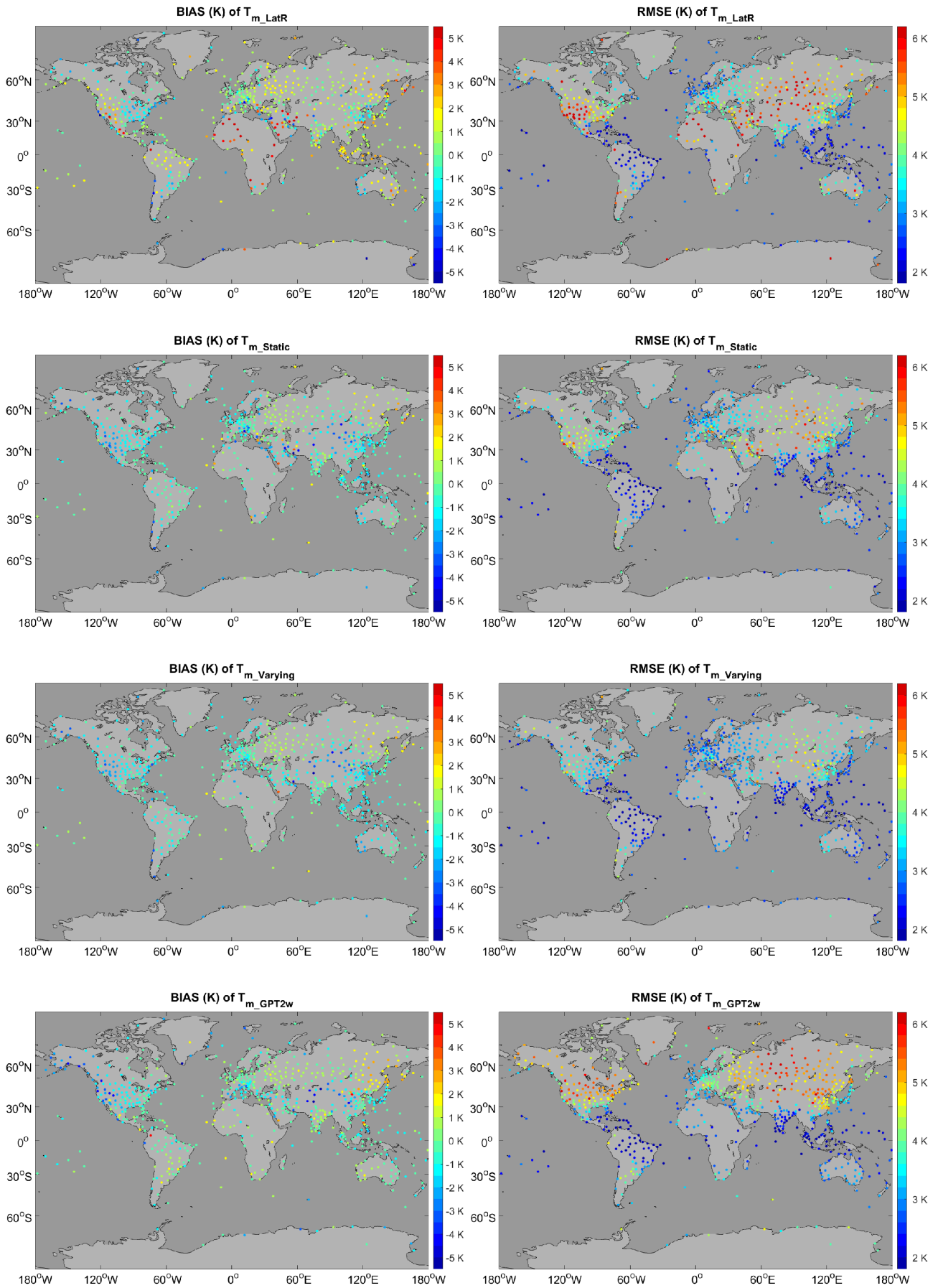
$$\cos \psi^i = \sin \varphi^i \sin \varphi + \cos \varphi^i \cos \varphi \cos(\theta^i - \theta) \quad (9)$$

Considering the fact that the reanalysis grids are definite, and every radiosonde site is in situ; we can compute the interpolation coefficients in equation (7) for all of the radiosonde stations. Then, these coefficients are stored as constants to avoid reduplicating the calculation.

Taking T_{m_RS} as the reference values, we calculated the biases and RMSEs of T_{m_Bevis} , T_{m_LatR} , T_{m_static} , $T_{m_varying}$, and T_{m_GPT2w} at each radiosonde site. The results are illustrated in figure 6. Obviously, in many regions, the Bevis equation has a bad precision with the absolute bias and RMSE both larger than 5 K. T_{m_LatR} can reduce the estimated biases in many areas, but the RMSEs remain large. Large biases still exist at quite a few radiosonde stations, e.g. in Africa or West Asia. T_{m_static} and T_{m_GPT2w} remove the large T_m biases at most of the radiosonde stations. $T_{m_varying}$ performs significantly better over the world, especially in the Middle East, North America, Siberia region, etc.

Detailed statistics of the distributions of the bias and RMSE using different models are shown in figure 7 and table 2. At over 97.37 % of the radiosonde stations, the biases of $T_{m_varying}$ are within -3~3 K. Large positive biases (> 3 K) nearly disappear in $T_{m_varying}$. In contrast, there are significant large biases in T_{m_Bevis} and T_{m_LatR} . Improvements in RMSE are more evident. The RMSEs of $T_{m_varying}$ are smaller than 4 K at over 91 % of the radiosonde sites, while few sites (<1 %) have RMSEs larger than 5 K. This is clearly better than the other models. In T_{m_Bevis} and T_{m_LatR} , there are more than 17 % of the radiosonde sites have RMSEs larger than 5 K. The overall performance of T_{m_GPT2w} is very close to T_{m_Bevis} , except that its absolute bias is smaller than the other T_s-T_m models.





260

Figure 6: (left) The bias and (right) the RMSE of the estimated T_m from respectively (top) the Bevis equation, (second) the latitude-related model, (third) our static global gridded model, (fourth) our time-varying global gridded model and (bottom) the GPT2w model at each radiosonde station. Reference data are the radiosonde data of the year 2016. Temperature unit is Kelvin.

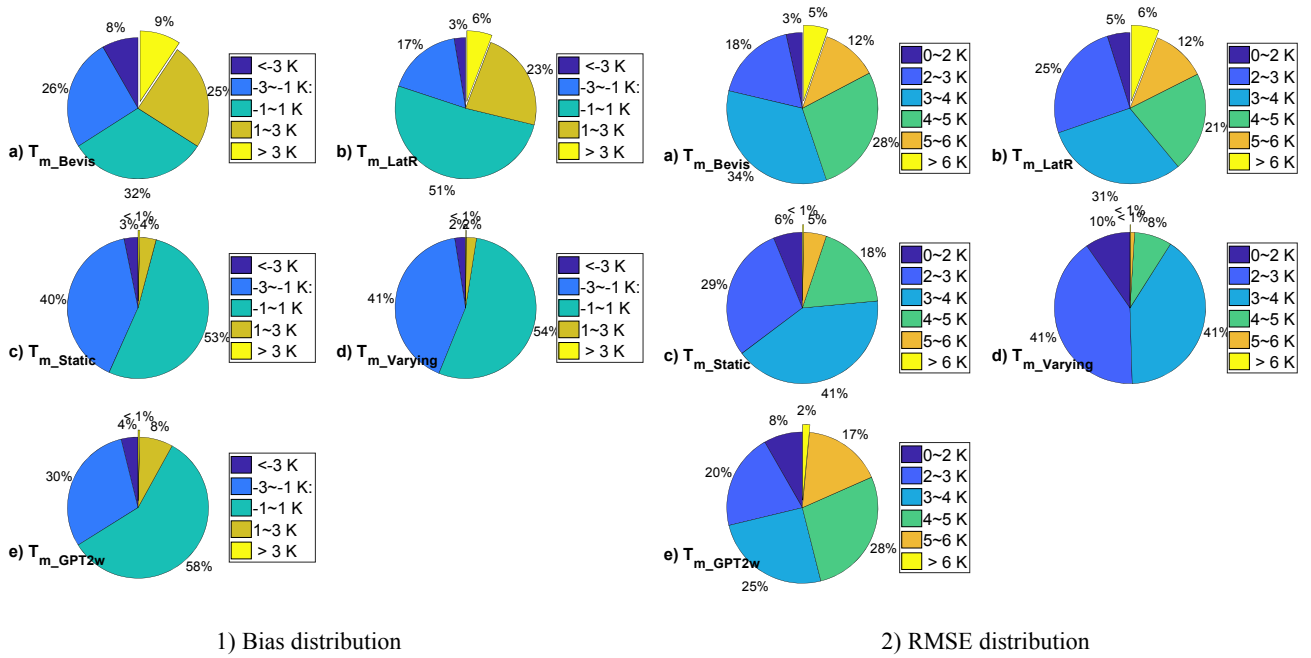


Figure 7: The distributions of (left) the biases and (right) the RMSEs of T_m compared with the radiosonde data at 723 stations in the year 2016. Temperature unit is Kelvin.

Table 2: Statistics of T_m estimates from different models. Reference data are the radiosonde T_m derivations.

Statistics	T_m Bevis	T_m LatR	T_m static	T_m varying	T_m GPT2w
Average value of absolute T_m bias (K)	1.88	1.30	1.13	1.08	1.06
Average value of T_m RMSE (K)	3.95	3.81	3.36	3.01	3.80
Average relative RMSE of T_m (%)	1.44	1.39	1.22	1.09	1.39
Max Relative RMSE of mean T_m (%)	3.69	4.26	2.40	2.19	4.31
% of sites with T_m RMSE < 4 K	55.19	61.00	76.49	91.01	53.94
% of sites with T_m Relative RMSE less than 1.5 %	59.47	64.73	78.01	89.76	56.43

To identify the superior T_m estimation model at each radiosonde site, we employed the following statistical tests under the assumption of a normal distribution of the estimated T_m error:

(1) First, Brown-Forsythe tests (Brown and Forsythe, 1974) of equality of variances were carried out at each site for estimating the T_m errors from two different models, e.g., model A and B . The purpose of this step is to determine whether there is significant variance difference between the T_m results. If the test rejects the null hypothesis at a 5 % significance level that the errors of model A and B have the same variance, the model with the smaller sample variance is regarded as the better one. However, if the test does not reject the homogeneity of variances, analysis of variance (ANOVA) is performed in the next step.

(2) ANOVA is a technique used to analyze the differences among group means (Hogg, 1987). It evaluates the null hypothesis that the samples all have the same mean against the alternative that the means are not the same. If the null hypothesis is rejected at a 5 % significance level, the T_m sample with smaller absolute mean value is believed to be better. Otherwise, we think that two models perform almost the same at this radiosonde site.

(3) After multiple tests and comparisons, the best model at each radiosonde station may be identified. However, at some sites no superior model can be confirmed. All the models are believed to have equivalent performances.

Finally, we counted the number of sites at which each T_m model respectively performed the best. The results are given in

table 3. The time-varying global gridded model is superior to the others at 434 radiosonde stations (60.03 % of all sites), while

the second-best estimation, T_{m_GPT2w} , is superior at only 12.86 % of the sites.

Table 3: Number of radiosonde sites at which the five global applied T_m estimation models respectively perform superiorly

Superior model	None	T_{m_Bevis}	T_{m_LatR}	T_{m_static}	$T_{m_varying}$	T_{m_GPT2w}
Number of sites	50	46	61	39	434	93

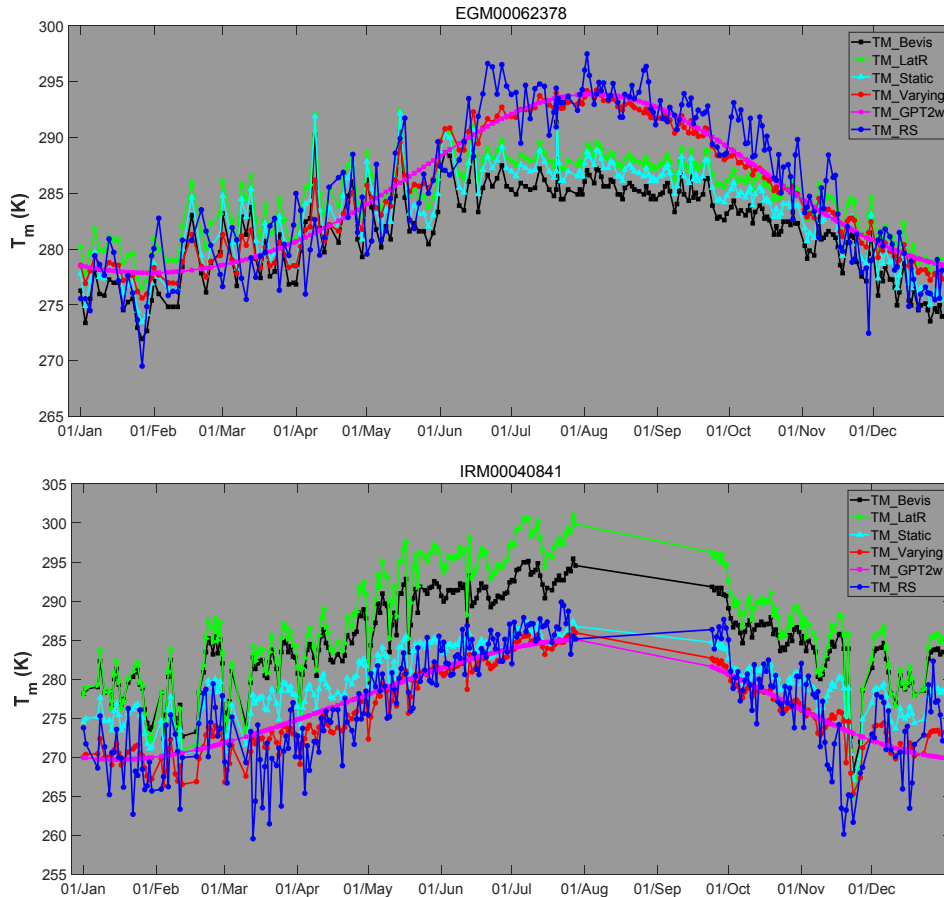
In figure 8, the T_m series at the IGRA station No.62378 (29.86° N 31.34° E, in Egypt) are given. We can see that large negative biases (< -5 K) between T_{m_Bevis} (or T_{m_LatR}) and T_{m_RS} exist. T_{m_static} performs only slightly better from July to October.

However, $T_{m_varying}$ and T_{m_GPT2w} can eliminate most of the seasonal errors. Different properties of T_m series appear at another

IGRA station No.40841 (30.25° N 56.97° E, in Iran). Some observation data are missing, but we can still see that there are large positive differences (> 5 K) between T_{m_Bevis} (or T_{m_LatR}) and T_{m_RS} throughout the year. The biases of T_{m_static} are much

smaller, but some large errors still appear in many months. The $T_{m_varying}$, however, performs as well as the T_m calculated from the radiosonde data, with small biases and capturing the variations well. The time series of T_{m_GPT2w} are smoother and cannot capture the fluctuations of the T_m time series, causing a worse accuracy than $T_{m_varying}$.

On the other hand, even $T_{m_varying}$ have large differences from T_{m_RS} at a few IGRA stations. This can be explained by the fact that our fitting analyses are based on the T_m values derived from ERA-Interim profiles. The quality of ERA-Interim data can be very poor in the regions with sparse observation data (Itterly et al., 2018).



300 **Figure 8: T_m series of T_{m_Bevis} , T_{m_LatR} , T_{m_static} , $T_{m_varying}$, T_{m_GPT2w} and T_{m_RS} at the IGRA station (top) No.62378 and (bottom) No.40841. Temperature unit is Kelvin.**

5. GPS-PWV retrieving experiments

GPS-PWV has different error sources with different properties. It is complicated to evaluate the GPS-PWV uncertainty here due to the lack of collaborated additional independent techniques to monitor water vapor at the GPS site.

305 5.1 Theoretical analysis of the GPS-PWV uncertainty

A comprehensive research on the uncertainty of GPS-PWV has been carried out by Ning et al. (2016). The uncertainties of the ZTD, ZHD and conversion factor Q have been studied in detail. The total uncertainty of GPS-PWV is:

$$\sigma_{PWV} = \frac{1}{Q} \sqrt{\sigma_{ZTD}^2 + \left(\frac{2.2767\sigma_{Ps}}{f(\varphi, H)} \right)^2 + \left(\frac{P_s\sigma_c}{f(\varphi, H)} \right)^2 + (PWV \cdot \sigma_Q)^2} \quad (10)$$

where σ_{PWV} , σ_{ZTD} , σ_{Ps} , and σ_Q are respectively the uncertainties of GPS-PWV, ZTD estimation, P_s observations and conversion factor Q . $\sigma_c=0.0015$ denotes the uncertainty of constant $C = 2.2767$ in equation (1), PWV is the value of GPS-PWV, and

$$\sigma_Q = 10^{-6} \rho_w R_v \sqrt{\left(\frac{\sigma_{k_3}}{T_m} \right)^2 + \sigma_{k'_2}^2 + \left(k_3 \frac{\sigma_{T_m}}{T_m^2} \right)^2} \quad (11)$$

where $\sigma_{k_3}=0.012 \times 10^5 \text{ K}^2 \text{ hPa}^{-1}$, $\sigma_{k'_2}=2.2 \text{ K hPa}^{-1}$, and σ_{T_m} denote respectively the uncertainties of k_3 , k'_2 and T_m in equation (4). The variation of σ_Q with the value of T_m and σ_{T_m} is depicted in figure 9. Assuming the T_m is 280 K, we find that the σ_Q increases by over 60 % (from 0.069 to 0.112) as the σ_{T_m} raises from 3.0 K to 5.0 K. However, the σ_Q is less sensitive to the value of T_m . The σ_Q raises only by 17.96 % (about from 0.061 to 0.075) as the value of T_m drops from 300 K to 270 K with $\sigma_{T_m} = 3.0 \text{ K}$.

Ning et al. (2016) assumed the T_m were obtained from NWP models so the uncertainty of T_m was set to be small ($\sigma_{T_m} = 1.1 \text{ K}$). However, as shown in section 4.3, the uncertainties of T_m from different T_m models are significantly larger at the radiosonde stations. For each radiosonde station, we calculated the mean value of T_m and assigned the σ_{T_m} with the RMSEs of T_m given in figure 6. Then we obtained the σ_Q in equation (11). Our statistics indicate that the σ_Q using our

varying T_s - T_m model decreases by average 19.26 %, 17.77 %, 7.79 % and 18.67 % with respect to the σ_Q respectively using the T_{m_Bevis} , T_{m_LatR} , T_{m_static} , and T_{m_GPT2w} . For example, at the IGRA station No.42724 (22.88° N 91.25° E, in India), σ_Q drops by 53 % from 0.141 of the T_{m_Bevis} to 0.066 of the $T_{m_varying}$.

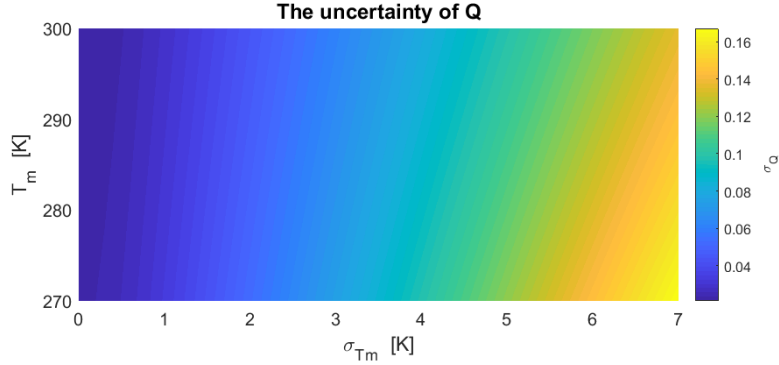


Figure 9. Variation of the uncertainty of Q with the value of T_m and the uncertainty of T_m

The uncertainty of Q will be propagated to the total uncertainty of GPS-PWV according to equation (10). We obtained the contributions of the different terms in equation (10) to the total GPS-PWV uncertainty. The contribution of one term is measured by the percentage it accounts for the total σ_{PWV} . The percentages are computed using formulas:

$$p_{ZTD} = \frac{(\sigma_{ZTD}/Q)^2}{\sigma_{PWV}^2}, p_{Ps} = \frac{[2.2767\sigma_{Ps}/(f(\varphi, H)Q)]^2}{\sigma_{PWV}^2}, p_C = \frac{[P_s\sigma_c/(f(\varphi, H)Q)]^2}{\sigma_{PWV}^2}, p_Q = \frac{(PWV \cdot \sigma_Q/Q)^2}{\sigma_{PWV}^2} \quad (12)$$

where p_{ZTD} , p_{Ps} , p_C and p_Q indicate respectively the contribution of the uncertainty associated with ZTD , P_s , constant C and factor Q to the total σ_{PWV} . Following the summaries of Ning et al. (2016), we assumed that $\sigma_{ZTD} = 4$ mm and $\sigma_c = 0.0015$. T_m identically equals to 280 K since the σ_Q is less sensitive to the value of T_m with respect to the σ_{Tm} . Table 4 gives five sets of the typical values which are assigned respectively to the σ_{Ps} , σ_{Tm} , P_s and PWV in equations (10)~(12).

Table 4. Different typical values for σ_{Ps} , σ_{Tm} , P_s and PWV

Set of typical values	σ_{Ps} [hPa]	σ_{Tm} [K]	P_s [hPa]	PWV [mm]
(a)	0.5	0 K ~ 7 K	1013.25	50
(b)	0.5	0 K ~ 7 K	850	50
(c)	0.5	0 K ~ 7 K	1013.25	20
(d)	5	0 K ~ 7 K	1013.25	50
(e)	5	0 K ~ 7 K	1013.25	20

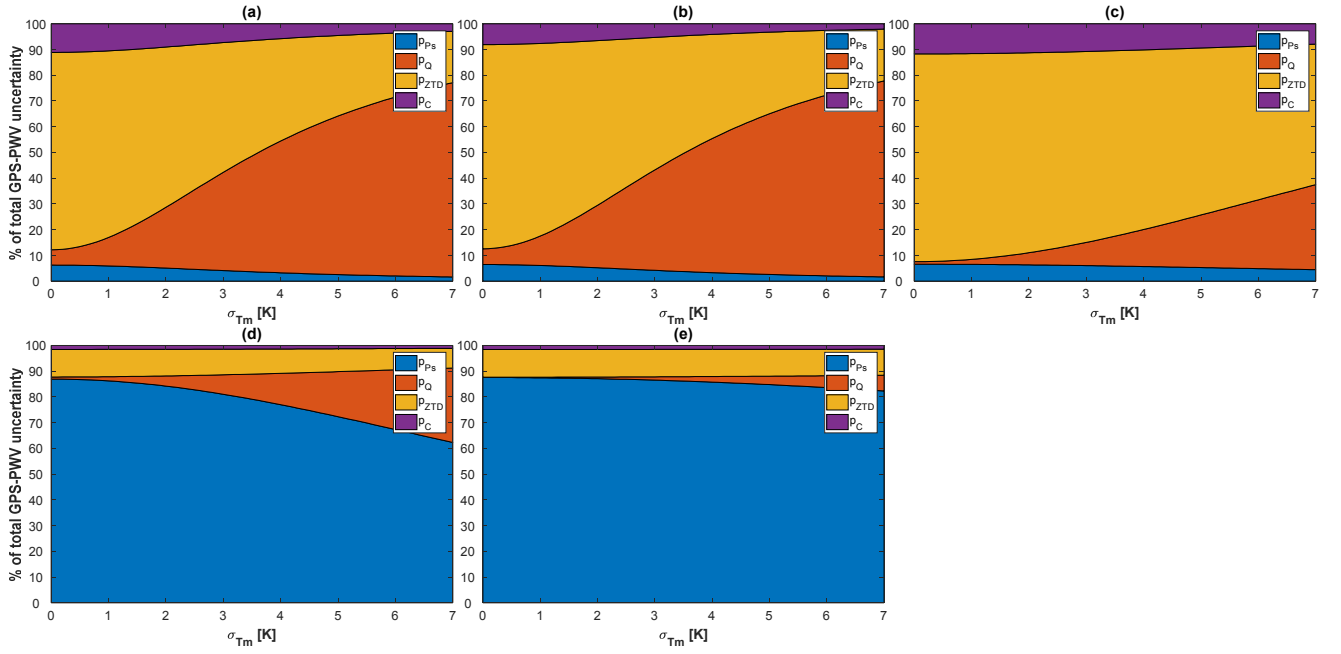


Figure 10. Contributions of different terms to the total uncertainty of GPS-PWV with the different typical values shown in table 4

The σ_{P_s} equals 0.2 hPa in Ning et al. (2016), however we enlarged its typical value to 0.5 hPa in consideration of the possible worse performance of the surface barometers. In figure 10, we illustrated the contributions of the terms in equation (12) based on the assumptions (a) ~ (e) in table 4. Some variation features of the contributions of different terms can be found from the comparisons between different subplots:

(1) No significant difference exists between the figure 10(a) and 10(b). Because of the small value of σ_c in equation (10), the σ_{PWV} is not sensitive to the value of P_s . Meanwhile, the uncertainty associated with σ_c contributes less than 10 % of the σ_{PWV} .

(2) With the typical values in table 4(a) and 4(b), a reduction of σ_{T_m} can reduce the p_Q significantly. For example in figure 10(a), the p_Q accounts for 69.54 % with $\sigma_{T_m} = 6$ K, and it declines to 38.19 % with $\sigma_{T_m} = 3$ K.

(3) As figure 10(c) shows, the uncertainty associated with σ_{ZTD} accounts for the main part of σ_{PWV} when the values of PWV and σ_{P_s} are not high. With the typical values in table 4(c), the p_{ZTD} can be up to 74.21 % with $\sigma_{T_m} = 3$ K. And the p_Q , however, can drop from 26.76 % to 9.00 % as the σ_{T_m} decreases from 6 K to 3 K. Although the p_Q is not large under this situation, a smaller σ_{T_m} can still reduce the contribution of σ_Q to the σ_{PWV} .

(4) The uncertainty associated with σ_{P_s} dominates the error budget of PWV when the σ_{P_s} is large. In figure 10(d-e), the p_{P_s} is over 80 % with $\sigma_{T_m} < 3$ K and $\sigma_{P_s} = 5$ hPa. In figure 10(d), the p_Q increases from 7.55 % to 23.19 % as the σ_{T_m} raises from 3 K to 6 K. However, in figure 10(e), the p_Q only grows from 1.29 % to 4.61 % with the same variation of σ_{T_m} .

355 Theoretical analyses on σ_{PWV} were also carried out at two representative stations. At the IGRA station No.42971 (20.25° N 85.83° E, in India), the mean value of PWV is 53.88 mm. The RMSEs of T_{m_Bevis} , T_{m_LatR} , T_{m_static} , $T_{m_varying}$, and T_{m_GPT2w} are respectively 4.30 K, 3.15 K, 2.41 K, 1.93 K and 1.97 K. The σ_{T_m} in equation (11) was replaced by the calculated RMSEs, and the p_{ZTD} , p_{P_s} , p_C and p_Q were generated with two typical values, 0.5 hPa and 5 hPa, assigned to the σ_{P_s} . With $\sigma_{P_s} = 0.5$ hPa, the p_C accounts for around 7 % while the p_{P_s} accounts for around 4 % of the total σ_{PWV} . By using different T_m estimations, the variations of p_C and p_{P_s} are both within 4 %. However, the p_Q varies more evidently. It accounts for average 55.69 %, 40.77 %, 30.70 %, 23.53 %, and 24.11 % of the σ_{PWV} respectively with the estimations of T_{m_Bevis} , T_{m_LatR} , T_{m_static} , $T_{m_varying}$, and T_{m_GPT2w} . The p_{ZTD} raises with the reduction of p_Q , e.g. from 36.23 % of T_{m_Bevis} to 62.53 % of $T_{m_varying}$. On the other hand, with $\sigma_{P_s} = 5$ hPa, the p_{P_s} accounts for more than 75 % of the σ_{PWV} while the p_Q decreases from 14.21 % of T_{m_Bevis} to 3.9 % of $T_{m_varying}$.

365 At another representative station, the IGRA station No.50557 (49.17° N 125.22° E, in Northeast China), the mean PWV is only 12.17 mm. The RMSEs of T_{m_Bevis} , T_{m_LatR} , T_{m_static} , $T_{m_varying}$, and T_{m_GPT2w} are respectively 5.16 K, 3.94 K, 3.54 K, 2.99 K and 5.10 K. We can see that the accuracy of T_m has been improved significantly. However, because of the low average value of PWV , the p_{ZTD} averagely contributes over 73.5 % of the σ_{PWV} while the p_Q averagely contributes less than 10.5 % assuming $\sigma_{P_s} = 0.5$ hPa and less than 1.5 % assuming $\sigma_{P_s} = 5$ hPa. But such discussion only concerns the average values. In fact, even at this station there are still some high values of PWV , for example at UTC 12:00 July 22th of 2016, the PWV reached 48 mm. For the observations with high PWV , the improvement in the accuracy of T_m can still exert significant positive impact on the reduction of p_Q .

It is worth mentioning that the uncertainty of ZHD may be underestimated in some situations. There are two reasons for this. Firstly, the calculation of ZHD assumes that the water vapor is not contributed to the mass of the atmosphere. The ZHD error introduced by this assumption is often negligible. But in some very wet regions, the mass of water vapor could produce significant errors to the ZHD calculation. Secondly and more importantly, the error of P_s in equation (1) can be very large sometime. Small σ_{P_s} is reasonable when the surface barometer is calibrated routinely and equipped together with the GPS antenna. However, if there were significant height difference between the GPS antenna and the barometer, the error of ZHD would increase significantly. Snajdrova et al.(2006) found that 10 m of height difference approximately causes a difference of 3 mm in the ZHD. On the other hand, P_s can be generated from NWP data if there were no nearby barometer to GPS site. The error of P_s could be very large using this method (Means and Cayan, 2013; Jiang et al., 2016). In these cases, the GPS- PWV error reduction due to the more precise T_m estimation will be very limited.

5.2 Impact of real T_m estimation

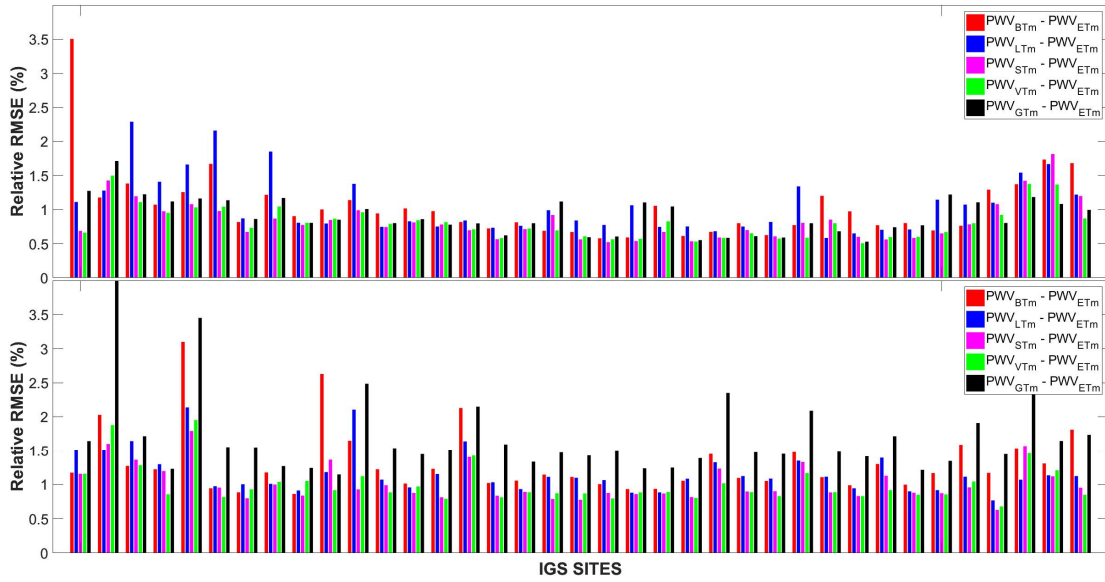
To study the impact of T_m on the real GPS-PWV retrieval, we first downloaded GPS ZTD products (Byun and Bar-Sever,

385 2009) at 74 IGS sites in the year 2016 from the NASA Crustal Dynamics Data Information System (CDDIS) ftp address (<ftp://cddis.gsfc.nasa.gov/pub/gps/products/troposphere/zpd>). These selected GPS sites were equipped with meteorological sensors so that the surface pressure and temperature measurements could also be obtained. ZHD was calculated using equation (1). It is subtracted from ZTD to obtain ZWD. Then, T_m was generated with six approaches: the first five T_m series were T_{m_Bevis} , T_{m_LatR} , T_{m_static} , $T_{m_varying}$, and T_{m_GPT2w} . The sixth T_m was integrated from the ERA-Interim profiles and interpolated to each 390 GPS site (Jiang et al., 2016; Wang et al., 2016). Finally, the GPS-PWV was generated from the ZWD and the six different T_m estimates leading to over one hundred compared points for each GPS-PWV series. We denoted these GPS-PWV sets as PWV_{BTm} , PWV_{LTm} , PWV_{STm} , PWV_{VTm} , PWV_{GTm} , and PWV_{ETm} . The only difference between these GPS-PWV estimations is the T_m estimation model; therefore, the impact of other errors is excluded.

The T_m from ERA-Interim is believed to be the most accurate among our T_m estimates at the selected GPS sites. We 395 therefore took the PWV_{ETm} as reference values to assess the other PWV. The relative RMSEs of PWV_{BTm} , PWV_{LTm} , PWV_{STm} , PWV_{VTm} and PWV_{GTm} at these selected stations were calculated and are illustrated in figure 11. The detailed statistics are given in table 5. The mean relative error of all sites drops from 1.18 % of the PWV_{BTm} to 0.91 % of the PWV_{VTm} . PWV_{VTm} has the minimum mean relative errors at 51.35 % of the sites, while PWV_{STm} is superior at 27.03 % of the sites. PWV_{STm} and PWV_{VTm} obtain relative RMSE smaller than 1.0 % at 55 sites, while only 28 sites of PWV_{BTm} , 31 sites of PWV_{LTm} and 22 sites 400 of PWV_{GTm} perform similarly. For example, at ALIC site (23.67° S 133.89° E, in Australia), with a mean PWV of approximately 23 mm, the relative RMSE dropped from 1.97 % of PWV_{BTm} to 1.10 % of PWV_{VTm} . The time series of the relative differences of PWV_{BTm} , PWV_{LTm} , PWV_{STm} , PWV_{VTm} , and PWV_{GTm} are given in figure 12. We found that some relative RMSEs could reduce more than 2 % from PWV_{BTm} to PWV_{VTm} . Obviously, PWV_{BTm} and PWV_{LTm} have larger relative errors throughout the year while the PWV differences are significantly larger only in the summer season (when the PWV values are 405 highest). Apparently, the T_m variations in summer are not modeled well by both Bevis model and the latitude-related model. PWV_{STm} eliminate those large differences but still retain some residual errors, which are removed by more than 0.5 mm in PWV_{VTm} . PWV_{GTm} has some large errors during the period from May to July. All of these results demonstrate that our time-varying model has precision advantages.

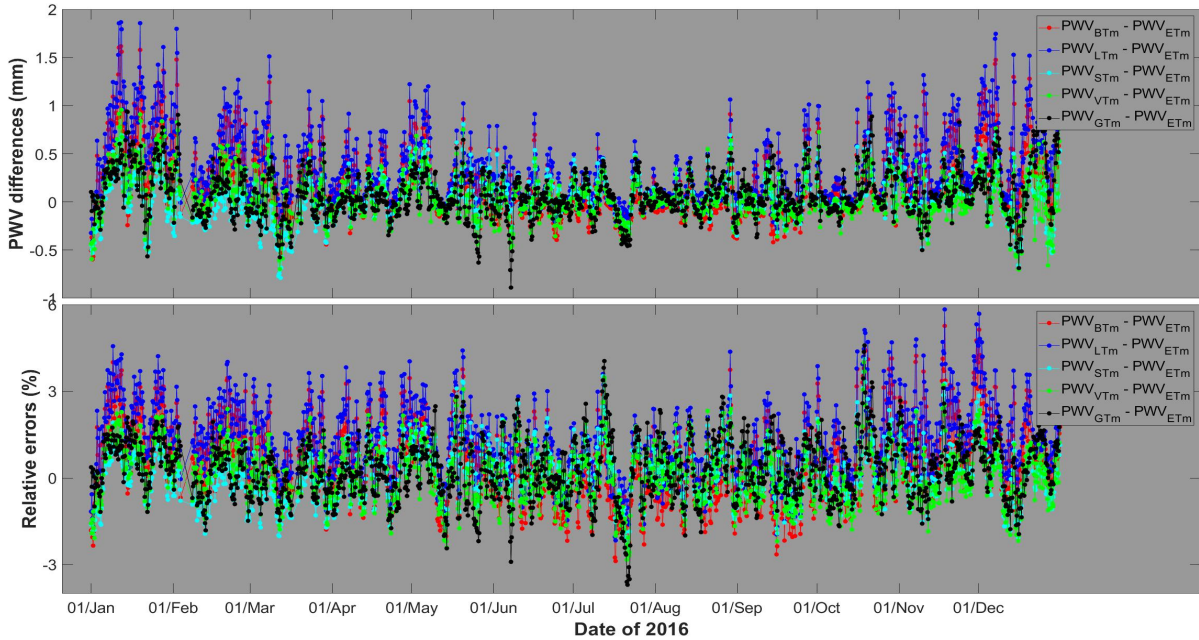
Table 5: Statistics about the relative errors of different PWV retrievals

Statistics	PWV_{BTm}	PWV_{LTm}	PWV_{STm}	PWV_{VTm}	PWV_{GPT2w}
Mean relative RMSE of all sites	1.18 %	1.12 %	0.93 %	0.91 %	1.32 %
Number of sites with relative errors < 1.0 %	28	31	55	55	22



410

Figure 11: Relative RMSEs of PWV_{BTm} , PWV_{STm} , PWV_{VTm} and PWV_{GTm} compared with PWV_{ETm} at 74 IGS stations in the year 2016



415

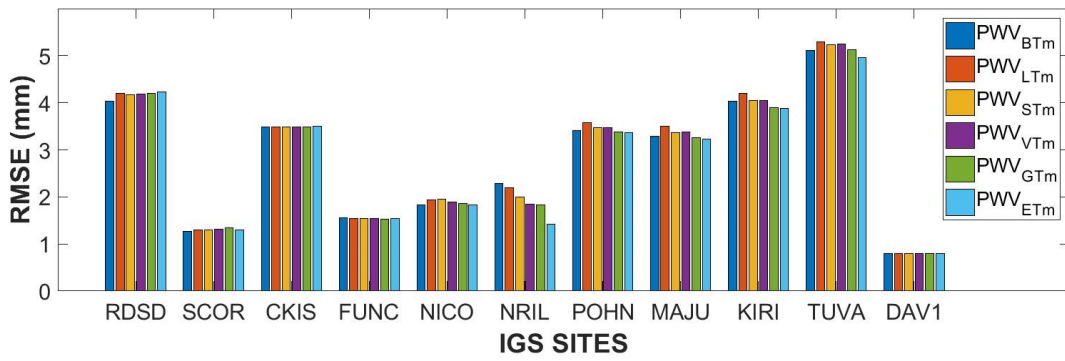
Figure 12: (top) PWV differences and (bottom) relative differences of PWV_{BTm} , PWV_{LTm} , PWV_{STm} , PWV_{VTm} and PWV_{GTm} compared with PWV_{ETm} at the ALIC station in the year 2016. PWV unit is mm.

5.3 Comparisons between GPS-PWV and radiosonde PWV

420

Among our selected 74 IGS sites, there are only 11 sites located within 5 km to a nearby IGRA radiosonde station. At these common stations, we generated PWV from the radiosonde data (PWV_{RS}) by adjusting the sounding profiles to the heights of IGS sites. It is worth noting that geoid undulation correction should be carried out on each IGS site geoid height (Jiang et al., 2016). Then, we compared PWV_{BTm} , PWV_{LTm} , PWV_{STm} , PWV_{VTm} , PWV_{GTm} , and PWV_{ETm} with PWV_{RS} . Figure 13 shows the statistics. The RMSEs of GPS-PWV are approximately 1~5 mm. Comparisons indicate that the RMSEs of different GPS-PWV retrievals are very close (differences < 0.2 mm) regardless of the applied T_m sources at most of the selected sites. This

means that other errors (e.g. ZTD estimation errors or sounding sensors errors) instead of the T_m make up the bulk of the differences between the GPS-PWV and the radiosonde PWV. Actually, each sounding does not represent the vertical sounding centered at the radiosonde site because of the complex path of the balloon. And GPS-PWV represents the averaged value of the water vapor zenithal projection from all the slant signal paths during the observation period. Such differences can introduce significant uncertainty to our comparisons. However, we still found obvious gaps between PWV at NRIL station (88.36° N 69.36° E, 4.1 km away from the IGRA station No.23078 in Russia). The RMSE decreases from 2.29 mm of PWV_{BTm} to 1.84mm of PWV_{VTm} and 1.42 mm of PWV_{ETm} . As shown in figure 14, the large PWV differences appear mainly from May to September. During those five months, the mean GPS-PWV difference to PWV_{RS} decreases by over 30 % from 2.52 mm of PWV_{BTm} to 1.67 mm of PWV_{VTm} , and the reductions of GPS-PWV error are mainly around 1~2 mm. This is attributed to the wetter atmosphere in these months. As indicated by the uncertainty analysis in section 5.1, the improvement in the accuracy of T_m can be translated in more error reduction in the GPS-PWV retrieval with higher value of PWV.



435 **Figure 13: RMSEs of the PWV_{BTm} , PWV_{STm} , PWV_{VTm} , PWV_{GTm} and PWV_{ETm} compared with the PWV_{RS} at 11 IGS stations in 2016. PWV unit is mm.**

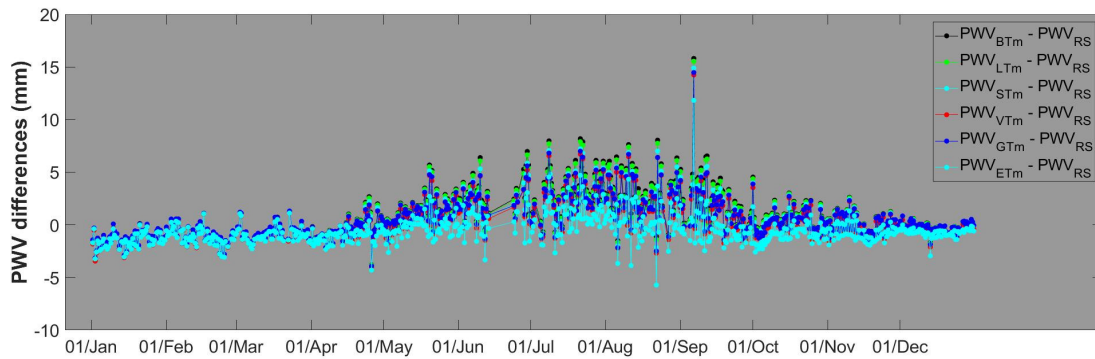


Figure 14: PWV differences of the PWV_{BTm} , PWV_{LTm} , PWV_{STm} , PWV_{VTm} , PWV_{GTm} and PWV_{ETm} compared with the PWV_{RS} at NRIL station in the year 2016. PWV unit is mm.

440 **6. Summary and conclusion**

We developed two global gridded T_s - T_m models which are respectively static and time-varying with a spatial resolution of $0.75^\circ \times 0.75^\circ$. The models are established by analyzing the ERA-Interim reanalysis datasets covering the year 2009~2012,

which indicated the significant spatial-temporal variations in T_s - T_m relationship as well as the radiosondes covering the same period. The annual, semiannual, and diurnal variations in T_s - T_m relationship are considered in the time-varying model. The
445 time-varying global gridded T_s - T_m model has a significant global precision advantage over the other global applied models, including the Bevis equation, the latitude-related model and the GPT2w model. Average RMSE of T_m reduces by approximately 1 K. At over 90 % of the radiosonde sites, our time-varying model has RMSE smaller than 4 K, while the RMSE larger than 5 K nearly disappear. On the other hand, in the Bevis model or in the latitude-related model, there are more than 17 % of the radiosonde sites having RMSE larger than 5 K. Multiple statistical tests at the 5 % significance level identified the
450 significant superiority of our varying model at more than 60 % of the radiosonde sites. Analyses at the specific stations demonstrate that the errors larger than 5 K in the estimated T_m series can be eliminated by our varying T_s - T_m model.

More precise T_m estimation can reduce around 20 % of the uncertainty in the conversion factor Q which maps GPS-ZWD to GPS-PWV, and the reduction can be even more than 50 % at some stations. The contribution of the uncertainty associated with Q to the total GPS-PWV uncertainty also declines by using a more precise T_m model. The reduction is related to the value
455 of PWV and the uncertainty of surface pressure. With GPS-PWV higher than 50 mm, the uncertainty associated with Q contributes more than 55 % of the uncertainty of GPS-PWV by using the Bevis equation and less than 25 % by using our varying T_s - T_m model, assuming the ZTD and the surface pressure are measured accurately respectively with the uncertainties of 4 mm and 0.5 hPa. However, the uncertainty in ZTD or in surface pressure would dominate the error budget of GPS-PWV (> 70 %) if the value of GPS-PWV were small or the uncertainty of surface pressure were large. In these cases, the uncertainty
460 associated with Q only contributes around 10 % of the GPS-PWV uncertainty or even smaller. Taking the GPS-PWV using ERA-Interim T_m estimates at 74 IGS sites as the references, we found that the GPS-PWV using our time-varying T_s - T_m model obtained the minimum mean relative error at 51.35 % of the sites, while the GPS-PWV using the static gridded T_s - T_m model is superior at only 27.03 % of the sites. The differences between GPS-PWV and radiosonde PWV are approximately 1~5 mm. And our varying T_s - T_m model can reduce 30 % (around 1~2 mm) of the error in GPS-PWV retrieval with respect to the Bevis
465 equation.

According to our experiments, we are confident that the time-varying global gridded T_s - T_m models presented here will help us to retrieve GPS PWV more precisely and to study the precise PWV variations in high temporal resolution. Matlab array file consisting of the global gridded coefficients in our model, as well as codes to interpolate coefficients at any given location, are provided as the supplement of this study.

470

Data sets

Radiosonde data: <ftp://ftp.ncdc.noaa.gov/pub/data/igra>

ERA-Interim Project: <https://doi.org/10.5065/D6CR5RD9>

GPS-ZTD Product: <ftp://cddis.gsfc.nasa.gov/pub/gps/products/troposphere/zpd>

475 Our model Supplement: <https://www.atmos-meas-tech-discuss.net/amt-2018-67/amt-2018-67-supplement.zip>

Acknowledgments

This study is supported by National Natural Science Foundation of China (No. 41604028), the Anhui Provincial Natural Science Foundation (No. 1708085QD83), and the Doctoral Research Start-up Funds Projects of Anhui University (No. J01001966). The authors thank European Centre for Medium-Range Weather Forecasts for providing the ERA-Interim dataset. We also thank the National Centers for Environmental Information for the IGRA datasets and International GNSS Service for the GNSS troposphere products.

480

Competing interests

The authors declare that they have no conflict of interest.

References

- 485 Adams, D. K., Barbosa, H. M. J., and De Los Rios, K. P. G.: A Spatiotemporal Water Vapor-Deep Convection Correlation Metric Derived from the Amazon Dense GNSS Meteorological Network, *Monthly Weather Review*, 145, 279-288, 10.1175/mwr-d-16-0140.1, 2017.
- Adler, B., Kalthoff, N., Kohler, M., Handwerker, J., Wieser, A., Corsmeier, U., Kottmeier, C., Lambert, D., and Bock, O.: The variability of water vapour and pre-convective conditions over the mountainous island of Corsica, *Quarterly Journal Of the Royal Meteorological Society*, 142, 335-346, 10.1002/qj.2545, 2016.
- 490 Bevis, M., Businger, S., Herring, T. A., Rocken, C., Anthes, R. A., and Ware, R. H.: GPS meteorology: Remote sensing of atmospheric water vapor using the global positioning system, *Journal of Geophysical Research: Atmospheres*, 97, 15787-15801, 10.1029/92JD01517, 1992.
- Bohm, J., Moller, G., Schindelegger, M., Pain, G., and Weber, R.: Development of an improved empirical model for slant delays in the troposphere (GPT2w), *Gps Solutions*, 19, 433-441, 10.1007/s10291-014-0403-7, 2015.
- 495 Brown, M. B., and Forsythe, A. B.: Robust Tests for the Equality of Variances, *Publications of the American Statistical Association*, 69, 364-367, 1974.
- Byun, S. H., and Bar-Sever, Y. E.: A new type of troposphere zenith path delay product of the international GNSS service, *J. Geodesy*, 83, 367-373, 10.1007/s00190-008-0288-8, 2009.
- 500 Campmany, E., Bech, J., Rodriguez-Marcos, J., Sola, Y., and Lorente, J.: A comparison of total precipitable water measurements from radiosonde and sunphotometers, *Atmospheric Research*, 97, 385-392, 10.1016/j.atmosres.2010.04.016, 2010.
- Chen, P., Yao, W. Q., and Zhu, X. J.: Realization of global empirical model for mapping zenith wet delays onto precipitable water using NCEP re-analysis data, *Geophys. J. Int.*, 198, 1748-1757, 10.1093/gji/ggu223, 2014.
- Ciesielski, P. E., Chang, W. M., Huang, S. C., Johnson, R. H., Jou, B. J. D., Lee, W. C., Lin, P. H., Liu, C. H., and Wang, J. H.: Quality-Controlled Upper-Air Sounding Dataset for TiMREX/SoWMEX: Development and Corrections, *Journal Of Atmospheric And Oceanic Technology*, 27, 1802-1821, 10.1175/2010jtecha1481.1, 2010.
- 505 Haase, J., Ge, M., Vedel, H., and Calais, E.: Accuracy and variability of GPS tropospheric delay measurements of water vapor in the western Mediterranean, *Journal of Applied Meteorology*, 42, 1547-1568, 10.1175/1520-0450(2003)042<1547:AAVOGT>2.0.CO;2, 2003.
- 510 Hogg, R. V., and Ledolter, J.: *Engineering Statistics*, Macmillan, New York, 1987.
- Itterly, K. F., Taylor, P. C., and Dodson, J. B.: Sensitivity of the Amazonian Convective Diurnal Cycle to Its Environment in Observations and Reanalysis, *Journal of Geophysical Research: Atmospheres*, 0, doi:10.1029/2018JD029251, 2018.
- Jade, S., and Vijayan, M. S. M.: GPS-based atmospheric precipitable water vapor estimation using meteorological parameters interpolated from NCEP global reanalysis data, *Journal of Geophysical Research-Atmospheres*, 113, 10.1029/2007jd008758, 2008.
- 515 Jiang, P., Ye, S. R., Chen, D. Z., Liu, Y. Y., and Xia, P. F.: Retrieving Precipitable Water Vapor Data Using GPS Zenith Delays and Global Reanalysis Data in China, *Remote Sensing*, 8, 10.3390/rs8050389, 2016.
- Karabatic, A., Weber, R., and Haiden, T.: Near real-time estimation of tropospheric water vapour content from ground based GNSS data and its potential contribution to weather now-casting in Austria, *Adv. Space Res.*, 47, 1691-1703, 10.1016/j.asr.2010.10.028, 2011.
- 520 Kealy, J., Foster, J., and Businger, S.: GPS meteorology: An investigation of ocean-based precipitable water estimates, *Journal Of Geophysical Research-Atmospheres*, 117, 10.1029/2011jd017422, 2012.
- Lan, Z., Zhang, B., and Geng, Y.: Establishment and analysis of global gridded Tm – Ts relationship model, *Geodesy and Geodynamics*, 7, 101-107, <https://doi.org/10.1016/j.geog.2016.02.001>, 2016.
- 525 Lee, J., Park, J.-U., Cho, J., Baek, J., and Kim, H. W.: A characteristic analysis of fog using GPS-derived integrated water vapour, *Meteorological Applications*, 17, 463-473, 10.1002/met.182, 2010.
- Li, X., Zhang, L., Cao, X. J., Quan, J. N., Wang, T. H., Liang, J. N., and Shi, J. S.: Retrieval of precipitable water vapor using MFRSR and comparison with other multisensors over the semi-arid area of northwest China, *Atmospheric Research*, 172, 83-94,

- 10.1016/j.atmosres.2015.12.015, 2016.
- 530 Liu, Z. Z., Li, M., Zhong, W. K., and Wong, M. S.: An approach to evaluate the absolute accuracy of WVR water vapor measurements inferred from multiple water vapor techniques, *Journal Of Geodynamics*, 72, 86-94, 10.1016/j.jog.2013.09.002, 2013.
- Lu, C. X., Li, X. X., Nilsson, T., Ning, T., Heinkelmann, R., Ge, M. R., Glaser, S., and Schuh, H.: Real-time retrieval of precipitable water vapor from GPS and BeiDou observations, *J. Geodesy*, 89, 843-856, 10.1007/s00190-015-0818-0, 2015.
- 535 Mahoney, K., Jackson, D. L., Neiman, P., Hughes, M., Darby, L., Wick, G., White, A., Sukovich, E., and Cifelli, R.: Understanding the role of atmospheric rivers in heavy precipitation in the Southeast US, *Monthly Weather Review*, 10.1175/MWR-D-15-0279.1, 2016.
- Means, J. D.: GPS Precipitable Water as a Diagnostic of the North American Monsoon in California and Nevada, *J. Clim.*, 26, 1432-1444, 10.1175/jcli-d-12-00185.1, 2013.
- 540 Means, J. D., and Cayan, D.: Precipitable Water from GPS Zenith Delays Using North American Regional Reanalysis Meteorology, *Journal of Atmospheric and Oceanic Technology*, 30, 485-495, 10.1175/jtech-d-12-00064.1, 2013.
- Ning, T., Elgered, G., Willen, U., and Johansson, J. M.: Evaluation of the atmospheric water vapor content in a regional climate model using ground-based GPS measurements, *Journal Of Geophysical Research-Atmospheres*, 118, 329-339, 10.1029/2012jd018053, 2013.
- 545 Ning, T., Wang, J., Elgered, G., Dick, G., Wickert, J., Bradke, M., Sommer, M., Querel, R., and Smale, D.: The uncertainty of the atmospheric integrated water vapour estimated from GNSS observations, *Atmos. Meas. Tech.*, 9, 79-92, 10.5194/amt-9-79-2016, 2016.
- Pacione, R., and Vespe, F.: Comparative studies for the assessment of the quality of near-real-time GPS-derived atmospheric parameters, *Journal of Atmospheric and Oceanic Technology*, 25, 701-714, 10.1175/2007jtecha935.1, 2008.
- 550 Perez-Ramirez, D., Whiteman, D. N., Smirnov, A., Lyamani, H., Holben, B. N., Pinker, R., Andrade, M., and Alados-Arboledas, L.: Evaluation of AERONET precipitable water vapor versus microwave radiometry, GPS, and radiosondes at ARM sites, *Journal Of Geophysical Research-Atmospheres*, 119, 9596-9613, 10.1002/2014jd021730, 2014.
- Raju, C. S., Saha, K., Thampi, B. V., and Parameswaran, K.: Empirical model for mean temperature for Indian zone and estimation of precipitable water vapor from ground based GPS measurements, *Ann. Geophys.*, 25, 1935-1948, 2007.
- 555 Rocken, C., Johnson, J., Van Hove, T., and Iwabuchi, T.: Atmospheric water vapor and geoid measurements in the open ocean with GPS, *Geophysical Research Letters*, 32, 10.1029/2005gl022573, 2005.
- Rohm, W., Yuan, Y. B., Biadeglne, B., Zhang, K. F., and Le Marshall, J.: Ground-based GNSS ZTD/IWV estimation system for numerical weather prediction in challenging weather conditions, *Atmospheric Research*, 138, 414-426, 10.1016/j.atmosres.2013.11.026, 2014.
- 560 Sheng, P., Mao, J., Li, J., Ge, Z., Zhang, A., Sang, J., Pan, N., and Zhang, H.: *Atmospheric Physics 2ed.*, Peking University Press, Beijing, 2013.
- Singh, D., Ghosh, J. K., and Kashyap, D.: Weighted mean temperature model for extra tropical region of India, *Journal of Atmospheric and Solar-Terrestrial Physics*, 107, 48-53, <http://dx.doi.org/10.1016/j.jastp.2013.10.016>, 2014.
- 565 Snajdrova, K., Boehm, J., Willis, P., Haas, R., and Schuh, H.: Multi-technique comparison of tropospheric zenith delays derived during the CONT02 campaign, *J. Geodesy*, 79, 613-623, 10.1007/s00190-005-0010-z, 2006.
- Song, J. J., Wang, Y., and Tang, J. P.: A Hiatus of the Greenhouse Effect, *Sci Rep*, 6, 9, 10.1038/srep33315, 2016.
- Van Baelen, J., and Penide, G.: Study of water vapor vertical variability and possible cloud formation with a small network of GPS stations, *Geophysical Research Letters*, 36, 10.1029/2008gl036148, 2009.
- 570 Wang, J. H., Zhang, L. Y., and Dai, A.: Global estimates of water-vapor-weighted mean temperature of the atmosphere for GPS applications, *Journal of Geophysical Research-Atmospheres*, 110, 10.1029/2005jd006215, 2005.
- Wang, X. M., Zhang, K. F., Wu, S. Q., Fan, S. J., and Cheng, Y. Y.: Water vapor-weighted mean temperature and its impact on the determination of precipitable water vapor and its linear trend, *Journal Of Geophysical Research-Atmospheres*, 121, 833-852, 10.1002/2015jd024181, 2016.
- 575 Wang, X. Y., Song, L. C., and Cao, Y. C.: Analysis of the weighted mean temperature of china based on sounding and ECMWF reanalysis data, *Acta Meteorol. Sin.*, 26, 642-652, 10.1007/s13351-012-0508-2, 2012.

Yao, Y., Zhang, B., Xu, C., and Yan, F.: Improved one/multi-parameter models that consider seasonal and geographic variations for estimating weighted mean temperature in ground-based GPS meteorology, *J. Geodesy*, 88, 273-282, 10.1007/s00190-013-0684-6, 2014a.

580 Yao, Y. B., Zhu, S., and Yue, S. Q.: A globally applicable, season-specific model for estimating the weighted mean temperature of the atmosphere, *J. Geodesy*, 86, 1125-1135, 10.1007/s00190-012-0568-1, 2012.

Yao, Y. B., Zhang, B., Xu, C. Q., and Chen, J. J.: Analysis of the global T(m)-T(s) correlation and establishment of the latitude-related linear model, *Chinese Science Bulletin*, 59, 2340-2347, 10.1007/s11434-014-0275-9, 2014b.